



Universiteit  
Leiden  
The Netherlands

## **Spectroscopic diagnostics of the mid-infrared features of the dark globule DC 314.8-5.1 with the Spitzer Space Telescope**

Kosmaczewski, E.; Stawarz, Ł.; Rocha, W.R.M.; Shenoy, S.S.; Karska, A.

### **Citation**

Kosmaczewski, E., Stawarz, Ł., Rocha, W. R. M., Shenoy, S. S., & Karska, A. (2022). Spectroscopic diagnostics of the mid-infrared features of the dark globule DC 314.8-5.1 with the Spitzer Space Telescope. *The Astrophysical Journal*, 934(2).  
doi:10.3847/1538-4357/ac7a42

Version: Publisher's Version  
License: [Creative Commons CC BY 4.0 license](https://creativecommons.org/licenses/by/4.0/)  
Downloaded from: <https://hdl.handle.net/1887/3561705>

**Note:** To cite this publication please use the final published version (if applicable).



# Spectroscopic Diagnostics of the Mid-infrared Features of the Dark Globule DC 314.8–5.1 with the Spitzer Space Telescope

E. Kosmaczewski<sup>1</sup> , Ł. Stawarz<sup>1</sup> , W. R. M. Rocha<sup>2</sup> , S. S. Shenoy<sup>3</sup> , and A. Karska<sup>4</sup> <sup>1</sup> Astronomical Observatory of the Jagiellonian University, ul. Orla 171, 30-244 Kraków, Poland; [emily@oa.uj.edu.pl](mailto:emily@oa.uj.edu.pl)<sup>2</sup> Laboratory for Astrophysics, Leiden Observatory, Leiden University, P.O. Box 9513, NL 2300 RA Leiden, The Netherlands<sup>3</sup> Space Science Institute, 4765 Walnut St., Rm. 203, Boulder, CO 80301, USA<sup>4</sup> Institute of Astronomy, Faculty of Physics, Astronomy and Informatics, Nicolaus Copernicus University, Grudziadzka 5, 87-100 Toruń, Poland

Received 2021 August 10; revised 2022 June 16; accepted 2022 June 17; published 2022 July 28

## Abstract

We present an analysis of the mid-infrared spectra, obtained from the Spitzer Space Telescope, of the dark globule DC 314.8–5.1, which is at the onset of low-mass star formation. The target has a serendipitous association with a B-type field star that illuminates a reflection nebula in the cloud. We focus on the polycyclic aromatic hydrocarbon (PAH) emission features prevalent throughout the mid-infrared range. The analysis of the spectra with the PAHFIT software as well as with the pypahdb package shows that (i) the intensities of PAH features decrease over distance from the ionizing star toward the cloud center, with some however showing a saturation at larger distances; (ii) the relative intensities of the 6.2 and 8.6 features with respect to the 11.2  $\mu\text{m}$  feature remain high throughout the globule, suggesting a higher cation-to-neutral PAH ratio of the order of unity; the breakdown from pypahdb confirms a high ionized fraction within the cloud; (iii) the pypahdb results display a decrease in large-PAH fraction with increased distance from HD 130079, as well as a statistically significant correlation between the large-size fraction and the ionized fraction across the globule; (iv) the 7.7 PAH feature displays a peak nearer to 7.8  $\mu\text{m}$ , suggesting a chemically processed PAH population with a small fraction of UV-processed PAHs; and (v) the H<sub>2</sub>S(0) line is detected at larger distances from the ionizing star. All in all, our results suggest divergent physical conditions within the quiescent cloud DC 314.8–5.1 as compared to molecular clouds with ongoing star formation.

*Unified Astronomy Thesaurus concepts:* Polycyclic aromatic hydrocarbons (1280); Infrared dark clouds (787); Interstellar medium (847); Molecular clouds (1072); Photodissociation regions (1223); Interstellar dust (836)

## 1. Introduction

Polycyclic aromatic hydrocarbons (PAHs), containing tens to hundreds of carbon atoms, are an abundant and ubiquitous component of the interstellar medium (ISM); although they are found in many different systems, ranging from molecular clouds in the Milky Way to distant active galactic nuclei, their origin and distribution are not fully understood (see, e.g., reviews by Tielens 2008; Joblin & Tielens 2011; Li 2020). PAHs can be observed via their infrared (IR) fluorescence through the vibrational modes, manifesting in particular in broad emission features at 3.3, 6.2, 7.7, 8.6, 11.3, and 12.7  $\mu\text{m}$ . This, however, heavily relies on ultraviolet (UV) radiation for excitation, and therefore quiescent properties of PAHs remain elusive.

There has been extensive modeling of PAHs in various environments, attempting to disentangle contributions of molecules with different sizes, charge states, or even structures and content to the IR radiative output at different wavelengths. It was shown that the 3.3 and 11.3  $\mu\text{m}$  features are predominantly due to neutral PAHs, while the 6.2, 7.7, and 8.6  $\mu\text{m}$  features are dominated by ionized PAHs; the relative intensity of the 6.2 and 7.7  $\mu\text{m}$  features, on the other hand, was argued to be sensitive to the number of carbon atoms in a molecule (e.g., Draine & Li 2001). Hence, the intensity ratio diagram “6.2/7.7 versus 11.3/7.7” is widely considered as a diagnostic tool enabling constraints on the distributions of PAH sizes and ionization

states in various astrophysical sources, especially in ones that can be spatially resolved by IR spectrometers (see Berné et al. 2007; Pineda & Bensch 2007; Visser et al. 2007; Rosenberg et al. 2011; Peeters et al. 2017; Boersma et al. 2018). More recently, however, other intensity ratios, such as 11.2/7.7 and 11.2/3.3, have been considered as more reliable proxies for the main characteristics of the PAH population, with the 3.3 feature being particularly sensitive to the number of carbon atoms in a molecule (Maragkoudakis et al. 2020).

The key factors determining plasma ionization, in addition to the amount of exciting emission, are the gas electron density and temperature. At the same time, the size distribution of PAHs is expected to be shaped by the ionizing continuum, as well as by shocks possibly present in the system (Siebenmorgen & Krügel 2010; Verstraete 2011; Boersma et al. 2014; Li 2020). As a result, in star-forming regions—which are the typical targets for resolved IR spectroscopy—PAHs undergo significant processing at early stages of the systems’ evolution, and so there is an observational bias in regard to probing the dust and PAH conditions in these systems following the onset of star formation.

Yet, the emission produced in the surroundings of young stars is not the only agent capable of ionizing the ISM or of causing grain destruction. In fact, lower-energy cosmic rays are often considered as an equally relevant source of ionization, particularly in the context of dense molecular clouds and the Galactic center region (e.g., Prasad & Tarafdar 1983; Padovani et al. 2009; Caselli et al. 2012; Indriolo & McCall 2013; Indriolo et al. 2015). In this context large PAHs can substantially modify the ionization balance in their environment via a charge transfer from interstellar ions (leading to the creation of PAH cations), or



Original content from this work may be used under the terms of the [Creative Commons Attribution 4.0 licence](https://creativecommons.org/licenses/by/4.0/). Any further distribution of this work must maintain attribution to the author(s) and the title of the work, journal citation and DOI.

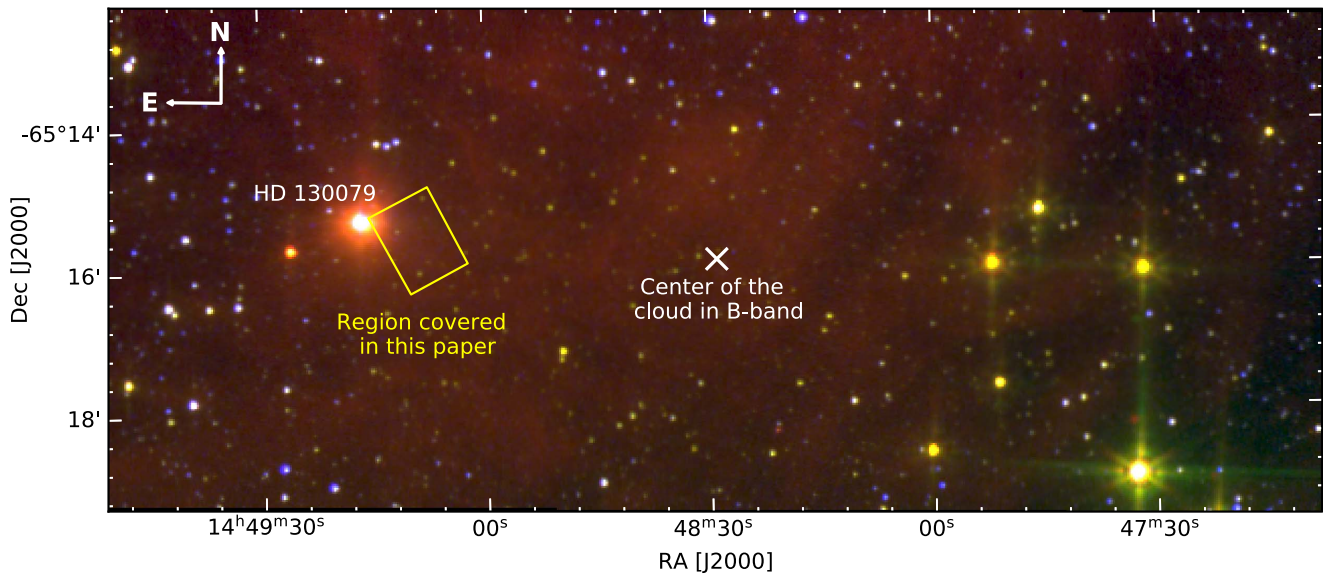


**Figure 1.** RGB image with a horizontal angular size of  $\sim 17'$  and a vertical angular size of  $\sim 7'$ , centered on the dark globule DC 314.8–5.1. The red, green, and blue colors are taken from Spitzer/IRAC 8.0  $\mu\text{m}$  and 5.8  $\mu\text{m}$  and the DSS1 blue band, respectively. The images are combined utilizing the APLpy package v2.0.2 (Robitaille & Bressert 2012; Robitaille 2019). HD 130079 can be identified as the bright star located left of center in the eastern boundary of the globule. The globule is the diffuse region in the center, obscuring and reddening the background starlight.

electron attachment (producing PAH anions), and subsequent mutual neutralization (Bakes & Tielens 1998; Dalgarno 2006; Verstraete 2011). In addition cosmic rays should be considered as a relevant agent responsible for destroying PAHs, especially smaller ones, and especially in dense clouds, where the competing processes of PAH destruction by interstellar shocks and UV emission are rather inefficient (Micelotta et al. 2011).

In this paper, we discuss the PAH features of a region at the eastern edge of DC 314.8–5.1, mapped with the Spitzer Space Telescope (Werner et al. 2004). Our work is motivated by a previous study by Whittet (2007), who identified the system as a compact and dense “dark globule” at the onset of low-mass star formation (see in this context the review by Bergin & Tafalla 2007). The distance and the parameters that depend on distance could be constrained relatively precisely by the serendipitous association of the cloud with a B-type field star, which illuminates a reflection nebula near its eastern boundary. The Spitzer Space Telescope observations analyzed here provide us the opportunity to also study the PAH features, at varying distances from the star, and at the same time from the center of the globule. In this way, we seek to diagnose the ionization level conditions and the dust grain distribution within the dense molecular cloud, *before* any formation of stars, and so they are not affected by the presence of young stellar objects.

The paper is organized as follows. In Section 2, we summarize the established properties of DC 314.8–5.1. In Section 3, we introduce the Spitzer Space Telescope observations targeting the system, and next in Section 4 we discuss the analysis performed on the Spitzer data. In Section 5 we present the analysis results regarding the PAH features and ratios; these results are further discussed in Section 6 and concluded in Section 7.

## 2. System Overview

DC 314.8–5.1 is a dark globule  $\sim 8' \times 5'$  in angular size, located approximately  $5^\circ$  below the Galactic plane,

R.A.(J2000) =  $14^{\text{h}}48^{\text{m}}29^{\text{s}}00$ , decl.(J2000) =  $-65^\circ 15'54''0$ , in the constellation of Circinus; see Figure 1. The system was originally identified in the Hartley et al. (1986) catalog of southern dark clouds and was selected from that catalog for further study. The globule is of particular interest due to its association with the field star HD 130079, embedded in its eastern boundary. HD 130079 is a 10th-magnitude, normal main-sequence star, with a well-established spectral type of B9V (Whittet 2007, and references therein); it illuminates a reflection nebula on the eastern boundary of the cloud.

The association of the star HD 130079 with DC 314.8–5.1 allows important physical characteristics of the system to be estimated. A review of the physical properties of HD 130079 and the dust responsible for extinction in the line of sight was carried out by Whittet (2007), with the goal of better constraining the distance to the star (and hence, to the cloud). Since this work was completed, new and far more accurate constraints on the distance to HD 130079 have become available as a result of parallax measurements by the Gaia mission. The parallax value for the star in the EDR3 data release (Gaia Collaboration et al. 2021) is  $2.2981 \pm 0.0194$  mas. This result corresponds to a distance of  $435 \pm 4$  pc, placing the star at a significantly greater distance compared with the photometric estimate of  $342 \pm 50$  pc deduced by Whittet (2007). The most likely cause of the discrepancy is an overestimate of the ratio of total to selective extinction in the earlier work, possibly resulting from contamination of the photometry by a fainter, redder star in the aperture. With the revised distance, the angular dimensions of the dark cloud ( $\sim 8' \times 5'$ ; Figure 1) correspond to a projected linear size of  $\sim 0.9$  pc  $\times$  0.6 pc. Using this result and other observed properties of the dark cloud, the mean core number density of hydrogen gas is  $\sim 10^4$  cm $^{-3}$ , and the total mass of the cloud is  $\sim 160 M_\odot$  (see Hetem et al. 1988; Whittet 2007).

DC 314.8–5.1 appears to be in a quiescent state prior to the start of star formation. There has been significant interest in verifying the validity of these so-called “starless cores,” but according to a study performed by Kirk et al. (2007) the probability of a misidentified core (i.e., that a “starless core” is

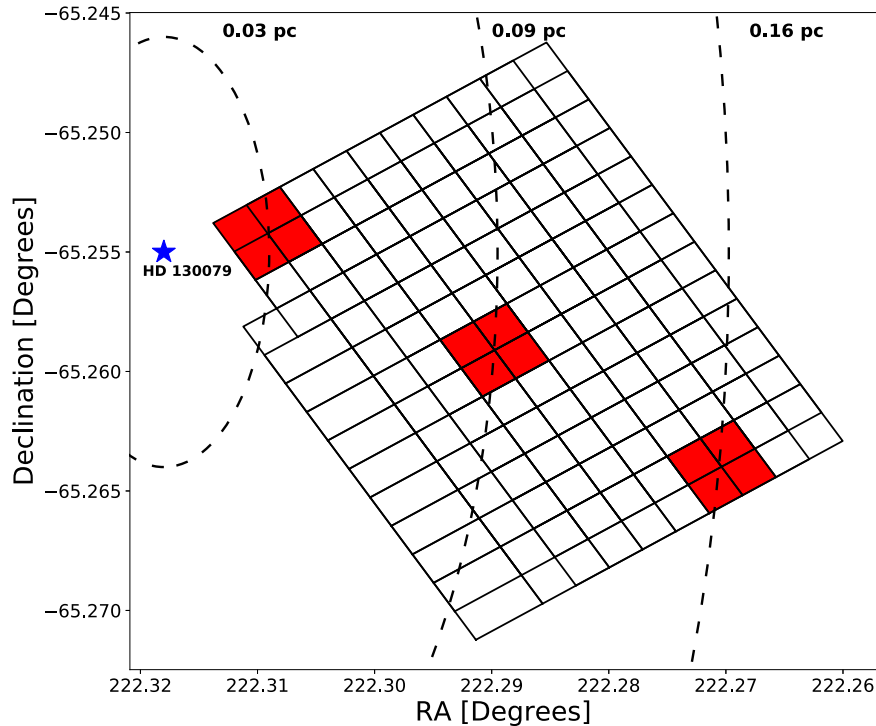


**Figure 2.** 117 overlapping Spitzer IRSMAP mid-IR (MIR) spectroscopic regions extracted from the eastern boundary of DC 314.8–5.1, with increasing distance from HD 130079. The extraction regions are overlapping to better account for subtle changes in features over distance. The red shaded regions mark three of the extraction regions that correspond to the spectra given in Figure 3, with the respective distance arcs marked by dashed lines. Each cube spans  $2 \times 2$  pixels with an angular width of  $\sim 5''$  per pixel, which at a distance of  $435 \pm 4$  pc (a systematic error of less than 1%) translates to a spatial size of a box width of  $\sim 0.02$  pc ( $\sim 10''$ ). The observational center of the cloud is positioned at R.A.(J2000) =  $14^{\text{h}}48^{\text{m}}29^{\text{s}}.00$ , decl.(J2000) =  $-65^{\circ}15'54''.0$ , with a projected distance of  $\sim 0.63$  pc from HD 130079. The spectral regions range from a distance of  $\sim 0.03$  pc to a distance of  $\sim 0.18$  pc from HD 130079.

not in fact starless but host to some stellar object) is low ( $\sim 5\%$ ). Proper verification for a starless core can be performed by utilizing the Multiband Imaging Photometer (MIPS) on board the Spitzer Space Telescope to search for sources embedded in a system (Kirk et al. 2007). A stellar consensus utilizing the Two Micron All Sky Survey (2MASS; Skrutskie et al. 2006) yielded only two potential young stellar object candidates in DC 314.8–5.1, one of which was excluded as an old star with significant dust reddening, out of a sample of 387 sources (Whittet 2007). The globule, therefore, was determined *not* to be a site of vigorous star formation, and as such is a valuable system to study the dynamics of a prestellar globule.

### 3. Spitzer Observations

Observational data for this work were provided by the Spitzer Space Telescope (proposal ID 50039; PI: D. Whittet), as acquired by the Infrared Spectrograph (IRS; Houck et al. 2004) mapping mode from the reflection nebula near the field star HD 130079. The IRS mapping observations, obtained through the Spitzer Heritage Archive, were used to investigate the relationship between the radiation from the field star and the corresponding PAH features within the globule.

The IRS mapping observations of the reflection nebula were obtained in both the short-low (SL) and long-low (LL) modules of IRS and cover the wavelength range of  $5.13$  to  $39.0 \mu\text{m}$ . These data have a resolving power of  $\simeq 60$ – $127$  and a signal-to-noise ratio  $S/N \simeq 20$ . We achieve the high  $S/N$  in a relatively short time:  $2 \times 60$  s in SL and  $2 \times 14$  s in LL. The slits are overlapped by  $1/2$  of the slit dimensions in both

directions, which mitigates artifacts due to bad and rogue pixels and results in a reduction of errors in flat-fielding.

## 4. Data Analysis

### 4.1. Reduction of Data Products

The data reduction procedure followed for the SL and LL spectroscopic data is similar to the CUBISM recipe outlined in the Spitzer Data Cookbook,<sup>5</sup> Recipe 10, with parameters appropriate for our data set. The CUBISM standard bad pixel generation was applied with the following values:  $\sigma_{\text{trim}} = 7$  and a minimum bad fraction equal to 0.5 for global bad pixels and equal to 0.75 for record bad pixels. Due to the source being a low-luminosity object, additional bad pixels were flagged visually before spectral extraction. One hundred and seventeen extraction regions of dimensions of  $2 \times 2$  pixels were defined around the field star HD 130079, within the reflection nebula, as visualized in Figure 2. Regions were selected such that the center of each new region was the edge of the previous region to account for subtle changes over distance. Spectral extraction was performed by selecting a region beginning on the star, of four pixels, and shifting the extraction region by one pixel for each new extraction (in both vertical and horizontal directions). Projected distances from the field star were calculated from the center of each selection cube. Each cube (i.e., each array of four neighboring pixels; see Figure 2) spans an angular width of  $\sim 10''$ , which at a distance of  $435 \pm 4$  pc (a systematic error of less than 1%) translates to a spatial size of  $\sim 0.021$  pc. In order to

<sup>5</sup> <https://irsa.ipac.caltech.edu/data/SPITZER/docs/>



extract spectra for the entire wavelength range, four cubes were built for each spatial extraction region, one for each spectral mode (i.e., SL1, SL2, LL1, and LL2) (Smith et al. 2007b).

Combination of the spectral modes (i.e., SL1, SL2, LL1, and LL2) was performed utilizing coding routines developed with Python (3.5.9 distribution<sup>6</sup>), and standard averaging methods involving propagation of errors. Differences in the continua of the SL and LL modes (prevalent in low-intensity regions) were taken into account by scaling the LL modes to the SL modes.

#### 4.2. Fitting Process for Data Products

Spectral decomposition of the IRSMAP observations was performed with the PAHFIT spectral fitting software (Smith et al. 2007a). PAHFIT utilizes a model consisting of the starlight and thermal dust continua in fixed-temperature bins, resolved dust features, prominent emission lines, and silicate dust extinction. This fitting was performed on all 117 extracted low-resolution spectra taken at varying distances away from HD 130079 (and therefore at decreasing distance to the cloud center; see Figure 2). The PAHFIT process results in images for each fit as well as text files denoting the central wavelength, the intensity, the respective errors for each line fit, and also the levels for the stellar and dust continuum fits. Specifically PAHFIT measures the starlight and dust continua at 300, 200, 135, 90, 65, 50, 40, and 35 K; 18 emission lines ( $H_2$ , Ar, S, Fe, Si, and Ne); 25 Drude profiles to fit the PAH features; and the extinction level. Due to the high excitation for the atomic lines, we did not expect or see any evidence of their presence in our sample and so all atomic lines were removed by fixing their normalization to zero during the fitting procedure (see Herbst & van Dishoeck 2009).

Figure 3 shows for illustration the three spectra extracted at three various distances from the star, after PAHFIT fitting. Data points are presented by black squares (with respective error bars), red curves indicate the stellar continuum, thick gray curves indicate the dust and stellar continuum, blue curves indicate the fitted dust features, violet curves indicate atomic and molecular spectral lines, dotted lines indicate components diminished by fully mixed extinction, and green curves represent the fully fitted model (Smith et al. 2007a). As is evident in Figure 3, the 5–20  $\mu\text{m}$  range is dominated by emission features, whereas the spectrum is almost featureless at longer wavelengths; we therefore focus on the 5–20  $\mu\text{m}$  spectrum in the following sections. Specifically we note the strongly ionized 6.2 and 7.7  $\mu\text{m}$  features, as well as the ionized 8.6  $\mu\text{m}$  feature, in addition to the strong 11.2–11.3  $\mu\text{m}$  neutral PAH feature.

Complementary fitting of the extracted spectra was performed utilizing the pypahdb<sup>7</sup> package (Shannon & Boersma 2018). Unlike the PAHFIT routine, which decomposed the 5–35  $\mu\text{m}$  low-resolution Spitzer spectra into dust continuum emission (modeled as a superposition of modified blackbodies), PAH features (fitted with phenomenological Drude profiles), and atomic/molecular lines (approximated as Gaussians), the pypahdb package utilizes the NASA Ames PAH IR Spectroscopic Database (see Bauschlicher et al. 2018 for an updated summary) to directly extract the ionization fraction and the size breakdown for the PAH molecules within the analyzed region by means of fitting the observed spectrum against a library of computed PAH spectra that contains data on thousands of PAH species.

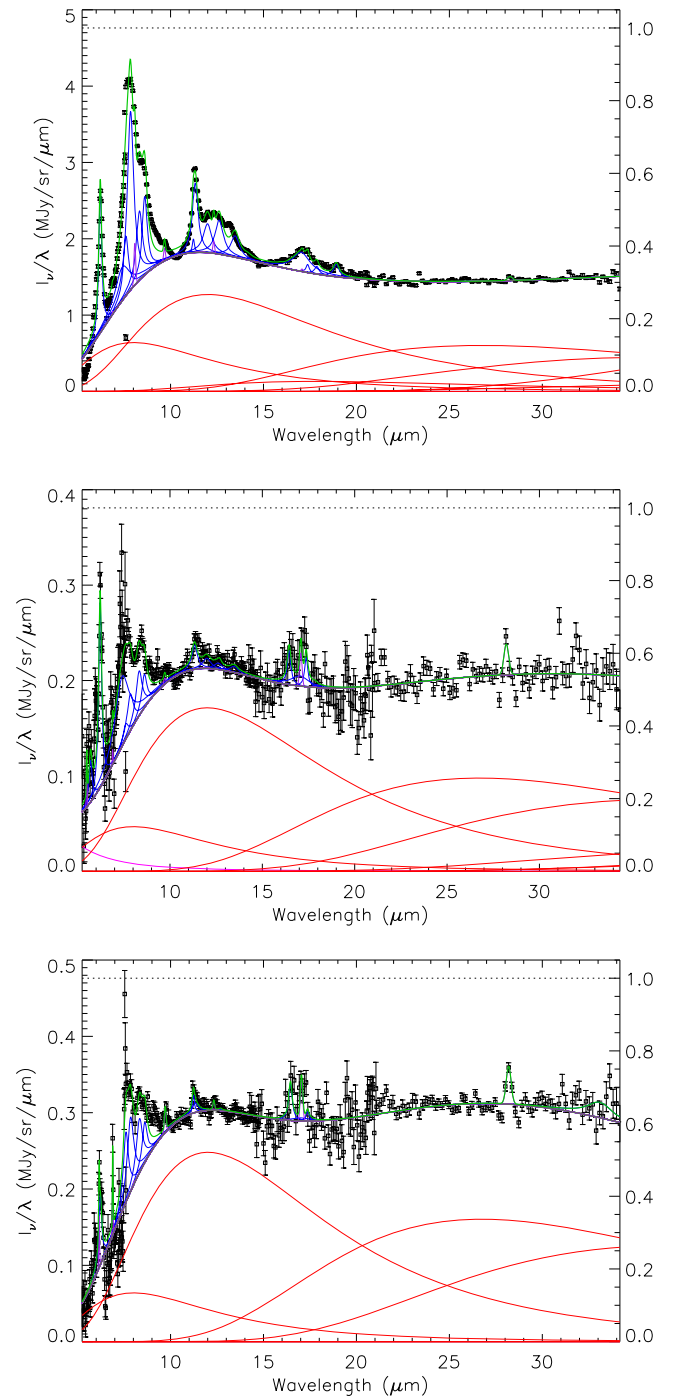


**Figure 3.** Fully fitted spectra extracted from the three regions at the projected distances of 0.03 pc, 0.09 pc, and 0.16 pc from the illuminating field star, HD 130079 (upper, middle, and lower panels, respectively); see Figure 2 for the physical extent of the extraction region for each spectrum. Spectral fitting of the regions was performed with PAHFIT (Smith et al. 2007a). The green curve represents the best fit; red curves represent the thermal dust continuum components, thick gray curves indicate the total dust and stellar continuum, blue curves indicate the fitted PAH features, and violet curves indicate atomic and molecular spectral lines. The dotted black lines (present in the top, middle, and bottom panels) denote the level of extinction (fully mixed) present (relative fraction presented on the right vertical axis).

For our study, we utilized pypahdb for each of our sampled regions for the Spitzer SL1 mode (i.e., 7.5–15  $\mu\text{m}$ ). We did not include the SL2 mode in this fitting as the inclusion of the additional segment from SL2 (6.5–7.5  $\mu\text{m}$ ) greatly reduced the quality of the fit, increasing residuals to  $>10$  MJy  $\text{sr}^{-1}$ .

<sup>6</sup> <https://docs.python.org/3/>

<sup>7</sup> <https://pahdb.github.io/pypahdb/>

Figure 4 presents the pypahdb fit for the extraction region located nearest to the field star HD 130079, at a distance of 0.03 pc, showing the respective breakdown of ionization and size, where large species are defined to have  $N_C > 40$ . The resulting spectral fits have a high  $S/N > 5$ , with only five regions having  $5 > S/N > 3$ , and only one region having an average residual equating to an  $S/N$  lower than  $3\sigma$ —as such it was removed from any further analysis.

#### 4.3. Extraction of Intensity Maps

Intensity maps were extracted from the Spitzer spectral cubes with CUBISM for selected features (Smith et al. 2007b). For each map the continuum was defined as the regions on either side of the feature, and removed, taking particular care in this procedure to not include any neighboring features or lines. The peak of the desired feature was then selected. This procedure produced a continuum-subtracted map of the averaged surface brightness in units of  $\text{MJy sr}^{-1}$ . In Figure 5 we present the resulting 6.2, 7.7, and 11.3  $\mu\text{m}$  PAH feature maps, created by defining the feature with the range for each peak as follows: 6.0–6.5  $\mu\text{m}$ , 7.3–7.9  $\mu\text{m}$ , and 11.2–11.4  $\mu\text{m}$ .

#### 4.4. Extinction Profile

For the inspection of line features within the dark globule DC 314.8–5.1, it is important to comment on the extinction within the sampled region. As given in Whittet (2007) the lower limit of the extinction of the cloud core is  $A_V \gtrsim 8.5$  mag; however, this is not the region that is sampled in our study. We are investigating the outskirts of the cloud from a 0.03–0.18 pc projected distance from HD 130079, which corresponds to a distance range from the core of DC 314.8–5.1 of 0.3–0.45 pc. Given however the extinction of 8.5 in the core of the cloud and the established relation  $N_{\text{H}_2}/A_V \simeq 9.4 \times 10^{20} \text{ cm}^{-2} \text{ mag}^{-1}$  (Hetem et al. 1988), and assuming the standard mass density profile for the cloud  $\rho(r) \propto r^{-1.3}$  (Cernicharo et al. 1985), we can estimate the extinction level within a certain distance probed in this paper, namely 0.3–0.45 pc from the center of the cloud, as 1.0–1.8 mag (corresponding to the  $\text{H}_2$  column density of  $\sim 1.0\text{--}1.7 \times 10^{21} \text{ cm}^{-2}$ ). The extinction within the sampled distances can therefore affect the PAH emission of the cloud, although we should still be able to probe the full depth of the targeted segment of the system. Obviously, given the simplicity of the abovementioned estimate, it is possible that the extinction in this region may be higher and we may only be seeing the surface of the cloud contributing to the PAH emission seen.

## 5. Results

### 5.1. Trends and Progressions

To a first approximation, one might expect a rather uniform distribution of PAH molecules within the relatively small region covered by the IRS mapping, and therefore that the PAH feature emission reflects, solely, the level of the ionizing continuum radiation. In other words, any spatial variation in the PAH features would be expected to be directly related to the emission of HD 130079, which is the dominant source of the UV photon flux within the sampled regions of the cloud and as such should decrease with projected distance from the star. However, trends in the feature intensities and intensity ratios observed in DC 314.8–5.1 appear to be more complex. Below

we inspect the individual fitted Drude profiles, along with the integrated PAH features, over distance. In the inspection of features only those with an  $S/N$  greater than 3 in at least 20% of the regions are included; here the  $S/N$  is calculated as, simply, the ratio of the fitted intensity of a given feature to the error in the fit.

First we inspect the individual Drude profile fits from PAHFIT over distance. The resulting trends can be generally divided into two major categories; in particular, as shown in Figure 6 and summarized in Table 1, we see either a single “inverse power law” scaling, or an “inverse power law + plateau” trend, i.e., an inverse power law behavior until a certain distance where the feature flattens out.

The individual PAH features can have multiple Drude profiles contributing to them, and so their integrated strength should be inspected rather than the individual Drude profiles. This concerns in particular the five main PAH features, namely 6.2, 7.7, 8.6, 11.3, and 17.0  $\mu\text{m}$ , for which the respective trends are given in Figure 7 and Table 2. Following the previous discussion, here the “power law” and “power law + plateau” categories are also represented. Note that for the integrated power trends we consider only the well-defined PAH features, excluding in particular the 8.3  $\mu\text{m}$  feature, for which PAHFIT returns a highly significant detection in terms of the Drude profile intensity (see Figure 6 and Table 1), even though this feature may be rather due to the blending of the neighboring 7.7 and 8.6 features (see the discussion in Peeters et al. 2017).

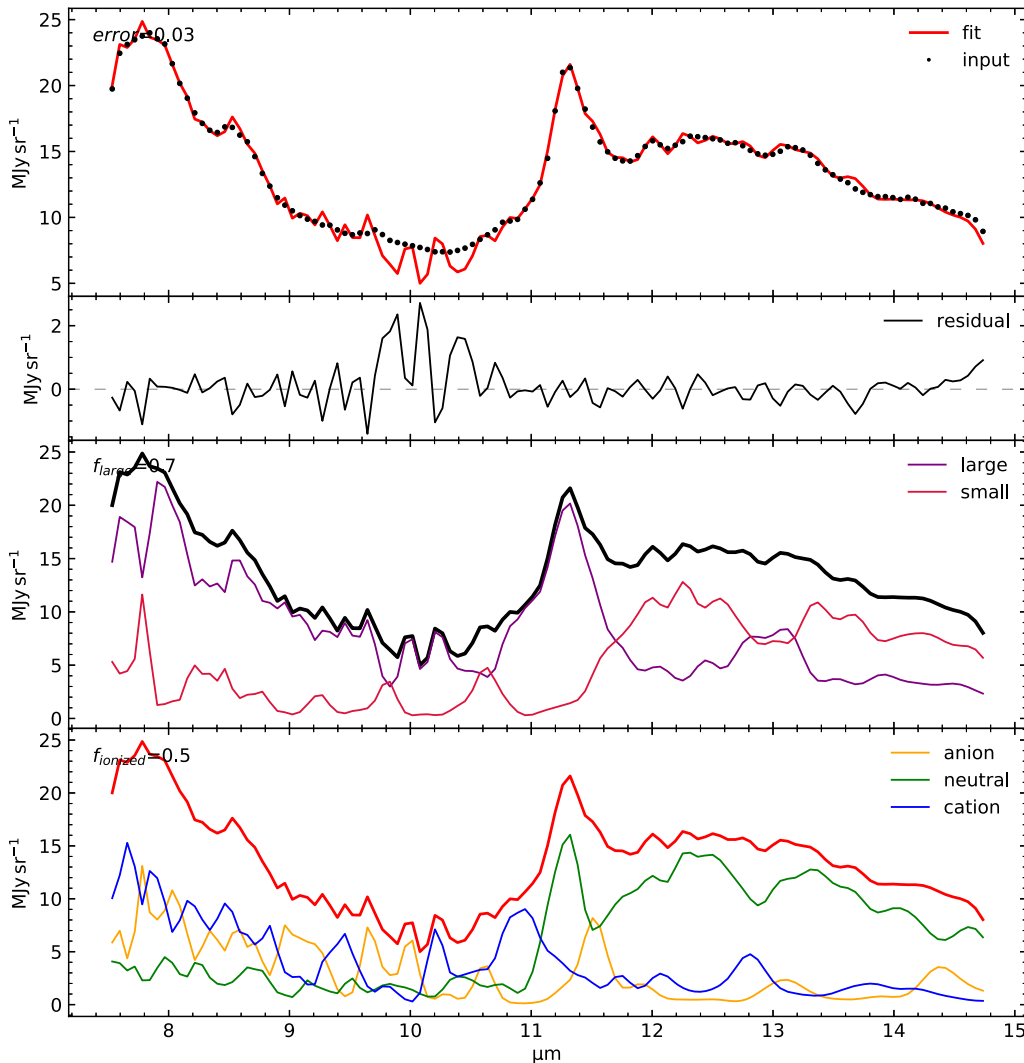
### 5.2. Individual Features and Lines

Figure 8 presents a zoomed-in view of the fully fitted 5.5–30.0  $\mu\text{m}$  segment of the spectrum for the region located at a 0.03 pc projected distance from HD 130079 (see the upper panel in Figure 3), highlighting the region that encompasses the majority of features. As shown, various profiles can contribute to single spectral features, and only by means of a detailed spectral fitting can one disentangle them. In the presentation of individual profiles we adopt the high significance/prevalence criterion, namely,  $S/N > 5$  detections in at least 20% of the regions. Figure 9 presents a more detailed zoomed-in view of the narrower 5.75–6.75, 6.75–10.5, 10–15, and 15–20  $\mu\text{m}$  segments of the spectrum for the same region, including model curves denoting various lines identified during the fitting procedure. The same decomposition was applied to all the analyzed 117 regions, and the results are given below in the following subsections.

#### 5.2.1. 5–7 $\mu\text{m}$ Features

In the upper left panel of Figure 9, the decomposition of the 6.2–6.3  $\mu\text{m}$  feature is shown. Our system has a consistent peak wavelength across the 117 regions of 6.22  $\mu\text{m}$ . Peeters et al. (2002) performed an investigation of the shift of the 6.3  $\mu\text{m}$  PAH feature due to the addition of a nitrogen atom in the molecule. The 6.3  $\mu\text{m}$  feature is represented by pure PAHs whereas the shifted peak around 6.2  $\mu\text{m}$  is emitted by substituted PAH species. Our observations are consistent with the findings presented in Peeters et al. (2002) for reflection nebulae, in which it is suggested that the shifting of the peak wavelength is due to the presence of nitrogen in the observed PAH molecules.

Another factor that can influence the positioning of the 6.2 peak is the presence of ice absorption around 6  $\mu\text{m}$  from water



**Figure 4.** The pyahdb (Shannon & Boersma 2018) fit of the SL1 mode from the nearest spectral region to HD 130079 at a projected distance of 0.03 pc. From top to bottom the individual panels represent the fully fitted spectrum with data points marked as black dots with respective errors (note here that the error bars are so significantly small as to not be easily visible), the residuals in the final fit, the breakdown of the PAH species sizes into large ( $N_C > 40$ ) and small, and the breakdown of the cation, neutral, and anion species.

ice. The ice features at  $6 \mu\text{m}$  can be confused with significant PAH features that are present at  $5.25$ ,  $5.7$ ,  $6.2$ , and  $7.7 \mu\text{m}$  (Peeters et al. 2002, and references therein). Indeed we see strong features at  $6.2$  and  $7.7 \mu\text{m}$  due to our PAH compounds, which makes it difficult to diagnose any potential ice absorption around  $6 \mu\text{m}$ .

The lack of water ice in this spectral range is consistent with what is expected for the cloud. The observations indicate that the ice formation threshold occurs for  $A_V$  above 1.6 mag toward different regions (e.g., Whittet et al. 2001; Chiar et al. 2011; Boogert et al. 2013; Whittet et al. 2013). Nevertheless, the visual extinction at the edges of DC 314.8–5.1 is estimated to be equal to  $1.08 \pm 0.2$  mag, without the foreground effect (Whittet 2007). Other molecules that show strong IR absorption features at around  $6 \mu\text{m}$ , such as HCOOH, H<sub>2</sub>CO, and CH<sub>3</sub>CHO, are more volatile than water, and thus would be formed in regions with larger extinction values ( $A_V > 3$  mag).

### 5.2.2. 7–10 $\mu\text{m}$ Features

The 7–10  $\mu\text{m}$  spectral region is complex and is decomposed into several Drude profiles. The statistically significant and

well-defined PAH features in this spectral selection are the ones centered at  $7.7$  and  $8.6 \mu\text{m}$ , as shown in Figure 9 upper right. The  $7.7 \mu\text{m}$  profile is fitted with three Drude profiles centered at  $7.4$ ,  $7.6$ , and  $7.8 \mu\text{m}$ . The peak of this feature is located longward of  $7.6 \mu\text{m}$ , which suggests a more dominant  $7.8 \mu\text{m}$  component. According to Peeters et al. (2002), this behavior is common among reflection nebulae, which typically display, in addition to the former, the shifted  $6.2 \mu\text{m}$  PAH feature, as is the case in DC 314.8–5.1 (see Section 5.2.1).

As discussed in Bregman & Temi (2005), PAHs in the diffuse ISM that have had long exposure to UV emission are dominated by a  $7.7 \mu\text{m}$  emission feature with a peak around  $7.6 \mu\text{m}$ . However, after integration into a cloud, these PAHs are chemically processed, and so the emission feature becomes shifted toward  $7.8 \mu\text{m}$ , and then back toward  $7.6 \mu\text{m}$  but only when having been exposed to an ionizing UV continuum in a reflection nebula. The fact that, in the analyzed segment of DC 314.8–5.1, we see a dominant emission component centered near  $7.8 \mu\text{m}$ , with a nonnegligible contribution from the emission at  $7.6 \mu\text{m}$ , implies that in addition to the “cloud-native,” chemically processed PAH population, we also see a

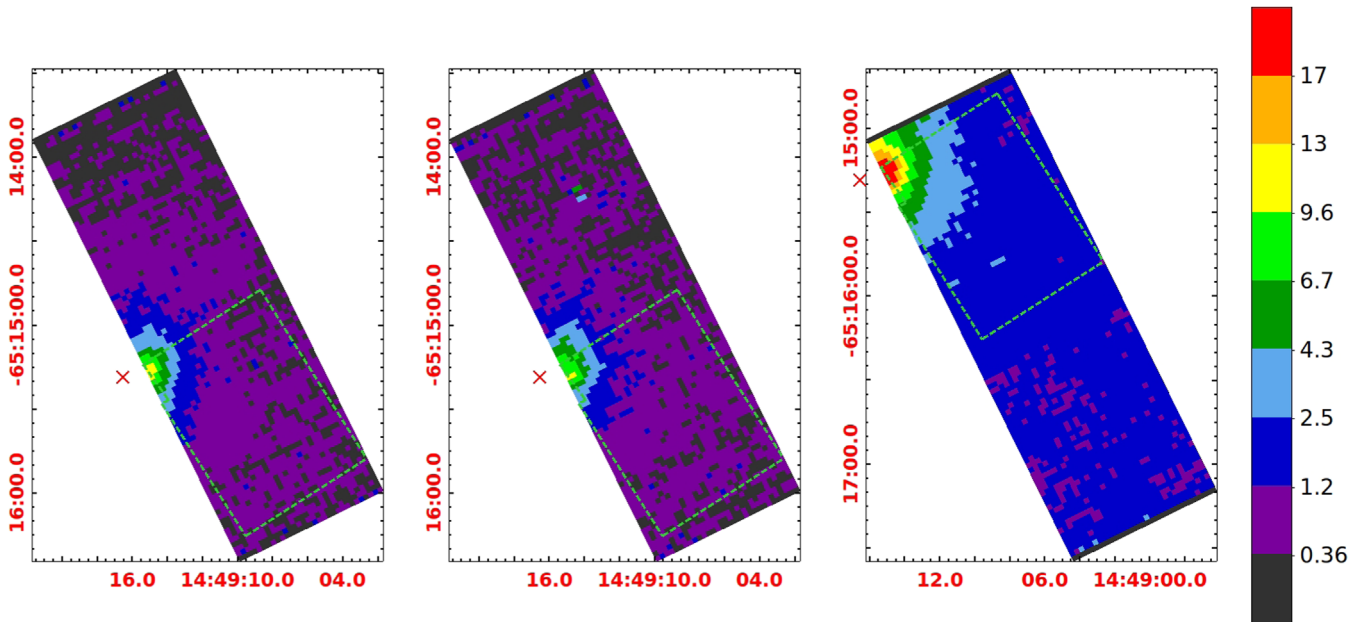


**Figure 5.** Square root scaled intensity maps of the continuum-subtracted PAH features: 6.2 (left), 7.7 (middle), and 11.3  $\mu\text{m}$  (right). The colorbar is set with a range across all the features of 0.1 to 21.5, with the maximum set by the 11.3  $\mu\text{m}$  feature and the minimum intensity set by the 6.2  $\mu\text{m}$  feature map. In all images the orientation is the same as that in Figure 1: north is oriented upward and east is oriented to the left. The green dashed lines delineate the extraction regions with the red cross indicating the optical center of HD 130079.

fraction of PAHs already being processed by the UV radiation of the neighboring star, HD 130079.

### 5.2.3. 10–15 $\mu\text{m}$ Features

A strong 11.2–11.3  $\mu\text{m}$  feature is commonly attributed to neutral PAHs within the cloud, and is correlated with many other PAH features. The profile in PAHFIT is comprised of two Drude profiles located at 11.2 and 11.3  $\mu\text{m}$ . Figure 9 bottom left shows that the 11.2 and 11.3 Drude profiles contribute to one PAH feature with a peak wavelength of  $\sim 11.25$ , but with a significantly more dominant contribution from the 11.3  $\mu\text{m}$  profile, and a lesser contribution from the 11.2  $\mu\text{m}$  profile. As is visible in Figure 4, this feature is dominated by large primarily neutral PAHs with the red wing of the feature being contributed to by anion PAHs. The 11.3  $\mu\text{m}$  Drude profile follows the inverse power law trend nicely, unlike the 11.2  $\mu\text{m}$  Drude profile. The overall integrated feature, however, does follow the power-law trend.

We note that PAHFIT does not fully converge in the 12–14  $\mu\text{m}$  region. Although the 12  $\mu\text{m}$  and 12.6  $\mu\text{m}$  PAH features are statistically significant, it is visible in Figure 9 that these lines are included in an attempt to fit the plateau present in this region and are not clear emission line detections. In Peeters et al. (2017), this plateau (10–15  $\mu\text{m}$ ) is attributed to a blending of irregular, small, and clustered PAHs emitted from the C–H bending modes (single, duo, trio, and quartet H atoms; see Allamandola et al. 1989; Bregman et al. 1989; Tielens 2008; Peeters et al. 2017, for an in-depth discussion of these plateau features). Due to PAHFIT not taking into account the plateau nature of this spectral section, we do not further consider the features between 12 and 14  $\mu\text{m}$ , as we cannot be confident with these detections.

### 5.2.4. 15–20 $\mu\text{m}$ Features

In the region past 15  $\mu\text{m}$  (see Figure 9 lower right panel), PAHFIT takes into account six Drude profiles at 15.9, 16.4, 17.0, 17.4, 17.9, and 18.9  $\mu\text{m}$  to fit the PAH features. The prominent (and as such statistically significant) features present here are the integrated PAH feature at 17.0  $\mu\text{m}$  and the PAH Drude profile at 18.9  $\mu\text{m}$ .

### 5.3. Dust Continuum

The PAHFIT process allows for eight thermal dust continuum components (featureless modified blackbodies), at fixed temperatures in the range 35–300 K; the set of best-fit amplitudes of all the components is expected to closely represent a smooth distribution of grain temperatures within the source (Smith et al. 2007a). Based on the fits obtained for each region extracted from the Spitzer IRS mapping data for DC 314.8–5.1, we can investigate the dominance of the eight model dust continuum components fit, with respect to the distance from the star (see Figure 10). Data points with  $S/N < 3$  are excluded, which comprise many of the lower-temperature components.  $S/N$  is taken from the fitted profile and the respective error in that fit.

First, we note that not all of the dust continuum components are required by the fitting procedure in all the 117 regions analyzed. The prevalence of dust components in the regions varies widely from  $\sim 5\%$  (e.g., the 35 and 40 K components), up to even  $>95\%$  in the case of the 200 and 300 K components. This indicates that the continuum emission of the dust, with the provided model temperatures, requires a full mix of lower- and higher-temperature blackbodies in the majority of sampled regions for a comprehensive fit of the continuum emission, in agreement with the findings by Whittet (2007).



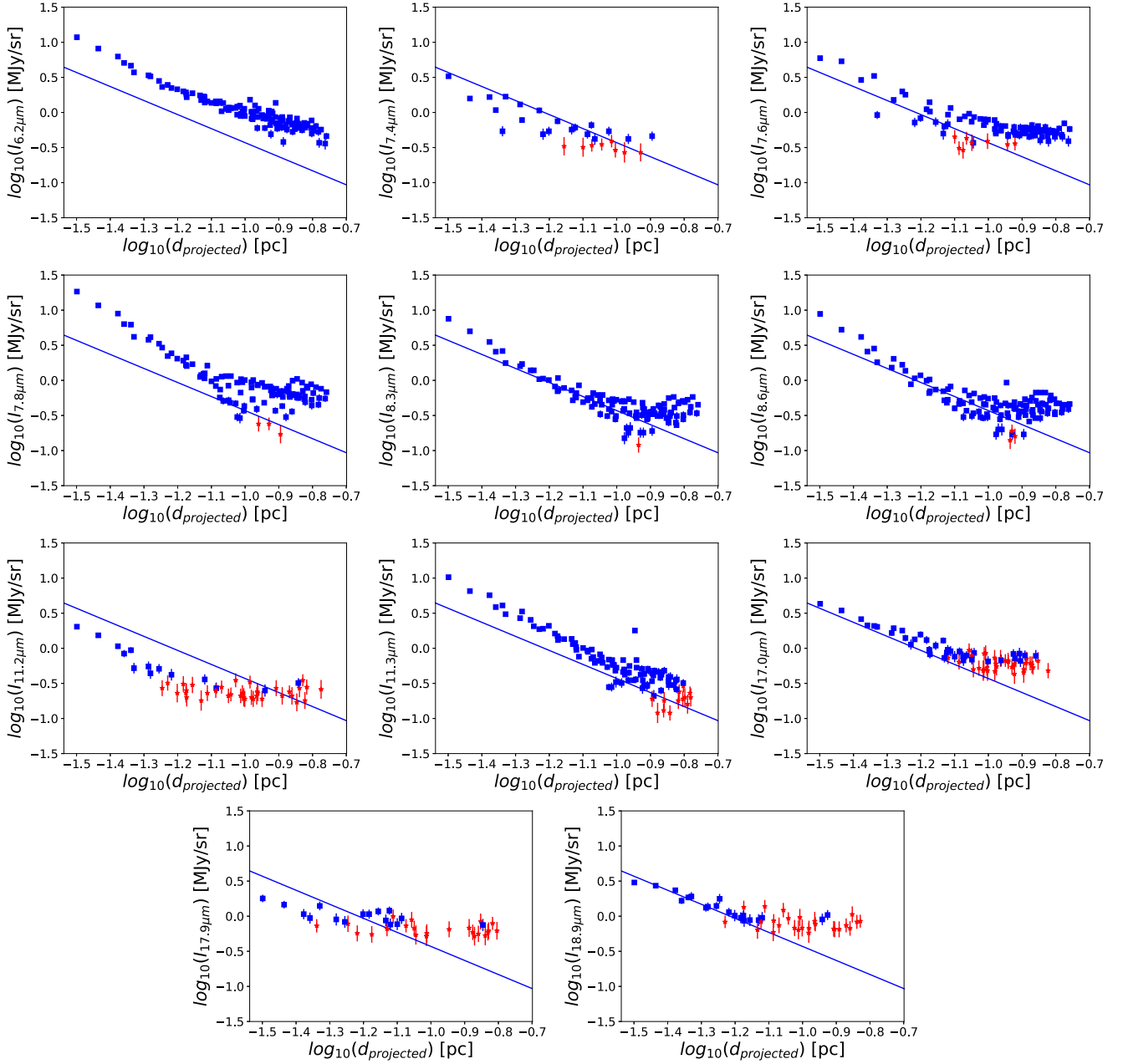


**Figure 6.** Logarithmic intensity of selected PAH features with respect to projected distance from the field star HD 130079. Blue lines represent the inverse square scaling (with arbitrary normalization), to guide the eye. S/N is marked in each panel by color and symbol with red stars marking the lowest,  $3 < S/N < 5$ , and blue squares marking all data points with  $S/N > 5$ .

In Figure 10, we plot the extracted relative normalization values for each temperature bin,  $\tau_m$ , as a function of distance from the star. These relative normalizations are defined in PAHFIT through the equation for the dust continuum intensity:

$$I_{\nu}^{(\text{dust})} = \sum_{m=1}^8 \tau_m \frac{B_{\nu}(T_m)}{(\lambda/\lambda_0)^2} \quad (1)$$

where  $B_{\nu}$  is the blackbody function,  $T_m$  denotes the selected thermal dust continuum temperatures, and  $\lambda_0 = 9.7 \mu\text{m}$  (Smith et al. 2007a). In the figure, each temperature bin is color-coordinated with the respective point for the fit shown.

Studies have shown that quiescent, nonactive cores of dust clouds have on average temperatures around 7–20 K, with colder temperatures dominating in the central regions (Bergin & Tafalla 2007). Molecular clouds, on the other hand, maintain on average temperatures around 20–30 K (Ward-Thompson 2002). In the case of DC 314.8–5.1, the most prominent dust continuum component corresponds to the temperatures of 40 and 35 K, having orders of magnitude higher normalizations than the hotter counterparts. These are, however, the lowest-temperature bins considered in PAHFIT, and no lower-temperature dust components are considered during the fitting because the dust below 35 K is too cold to make any contribution at  $\lambda < 40 \mu\text{m}$  (Smith et al. 2007a).

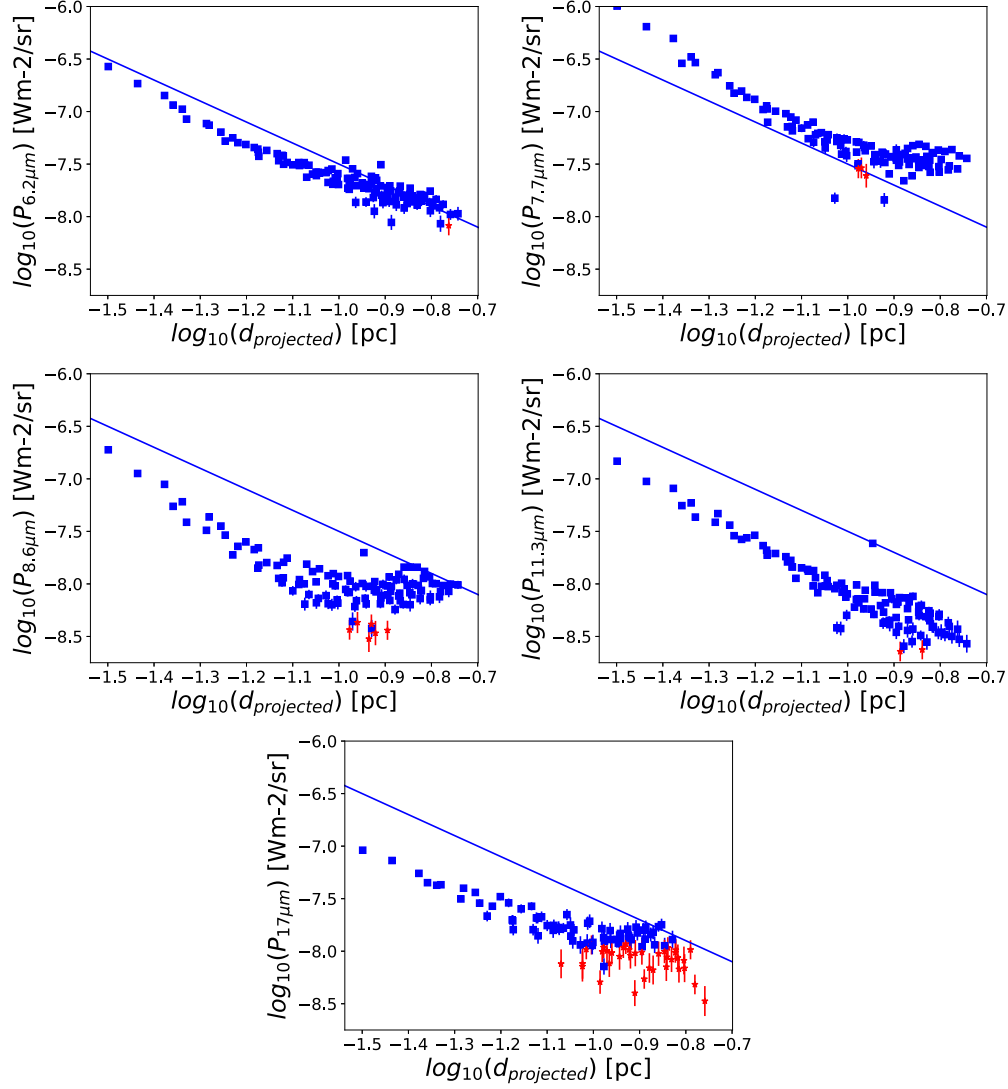


**Figure 7.** Logarithmic intensity of the integrated power of the main PAH features with respect to projected distance from the field star HD 130079. Blue lines represent the inverse square scaling (with arbitrary normalization), to guide the eye. S/N is marked in each panel by color and symbol with red stars marking the lowest,  $3 < S/N < 5$ , and blue squares marking all data points with  $S/N > 5$ .

**Table 1**  
PAH Drude Profiles

Feature	Wavelength ( $\mu\text{m}$ )	Max Intensity ( $\text{MJy sr}^{-1}$ )
<b>The “Inverse Power Law” Category</b>		
PAH 6.2	6.22	$12.3 \pm 0.002$
PAH 7.4	7.42	$4.26 \pm 0.009$
PAH 11.3	11.3	$10.2 \pm 0.003$
<b>The “Inverse Power Law + Plateau” Category</b>		
PAH 7.6	7.6	$5.39 \pm 0.010$
PAH 7.8	7.85	$18.5 \pm 0.002$
PAH 8.3	8.33	$7.69 \pm 0.003$
PAH 8.6	8.61	$8.84 \pm 0.003$
PAH 11.2	11.2	$2.05 \pm 0.023$
PAH 17.0	17.0	$4.67 \pm 0.020$
PAH 17.9	17.8	$2.06 \pm 0.046$
PAH 18.9	18.9	$3.46 \pm 0.028$

**Note.** Column (1)—PAH Drude profile designation; Column (2)—central wavelength as fit by PAHFIT; and Column (3)—maximum intensity out of the 117 regions as fit by PAHFIT.

## 6. Discussion

### 6.1. PAH Ionized Fraction

Boersma et al. (2014) derived a relation between the number density ratio of PAH cations to neutrals,  $n_{\text{PAH}^+}/n_{\text{PAH}^0}$ , and the main physical parameters in the system, including the gas temperature  $T$ , the ionizing radiation field  $G_0$ , the free electron number density  $n_e$ , and the PAH number of carbon atoms  $N_C$ , namely

$$\frac{n_{\text{PAH}^+}}{n_{\text{PAH}^0}} \simeq 5.11 \times 10^{-6} N_C^{1/2} G_0 T^{1/2} n_e^{-1}, \quad (2)$$

where  $T$  is given in kelvin,  $G_0$  is in Habing field units, and  $n_e$  is in  $\text{cm}^{-3}$ . Note that the PAH ionization parameter is often defined as  $\chi \equiv G_0 T^{1/2} n_e^{-1}$ , so that for the exemplary  $N_C \simeq 50$  one has  $(n_{\text{PAH}^+}/n_{\text{PAH}^0}) \sim 0.37 (\chi/10^4)$ .

For rough estimates regarding the cation-to-neutral PAH ratio in DC 314.8–5.1 subjected to the ionizing photon field of HD 130079, we therefore make the following approximations. First, we assume a dominant gas temperature component of  $T \sim 800$  K, according to the discussion by Boersma et al. (2018) for the

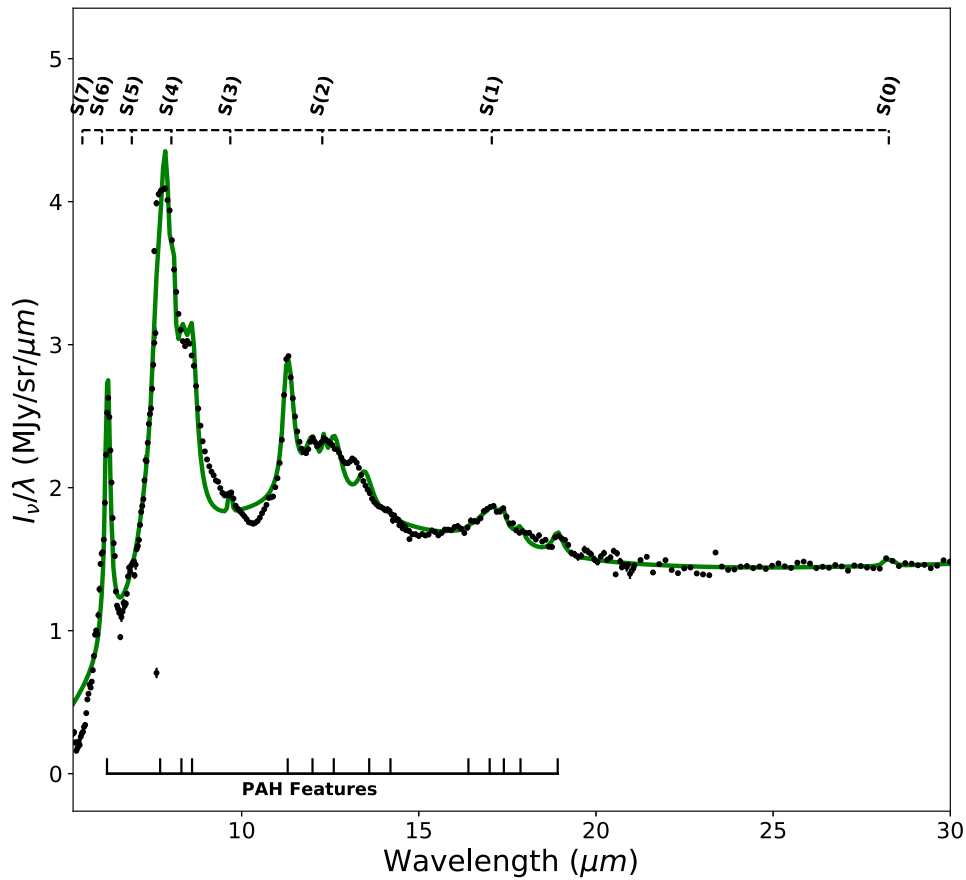


**Figure 8.** A zoomed-in view of the 5.5–30.0  $\mu\text{m}$  segment of the spectrum for the region located at a 0.03 pc projected distance from HD 130079 (see the upper panel in Figure 3), highlighting the region encompassing the majority of PAH activity. A green solid line indicates the fully fitted model extracted from PAHFIT (Smith et al. 2007a). Black points mark the real data points with error bars included. A dashed line at the top of the plot marks the S(0–7) rotational lines of  $\text{H}_2$  included in the PAHFIT fitting process, and a solid line at the bottom of the plot indicates all of the PAH features included in the fitting process (within the 5.5–30.0  $\mu\text{m}$  segment).

**Table 2**  
Integrated PAH Features

Feature	Wavelength ( $\mu\text{m}$ )	Max Power ( $\text{W m}^{-2} \text{sr}^{-1} \times 10^{-9}$ )
<b>The “Inverse Power Law” Category</b>		
PAH 6.2	6.2–6.3	$279 \pm 1.38$
PAH 11.3	11.2–11.4	$146 \pm 0.712$
<b>The “Inverse Power Law + Plateau” Category</b>		
PAH 7.7	7.3–7.9	$1070 \pm 5.41$
PAH 8.6	8.6–8.7	$189 \pm 1.35$
PAH 17.0	16.4–17.9	$99.5 \pm 2.87$

**Note.** Column (1)—PAH feature designation; Column (2)—central wavelength as fit by PAHFIT; and Column (3)—maximum power measured out of 117 regions as fit by PAHFIT.

photodissociation region (PDR) in NGC 7023. For the free electron number density, on the other hand, we follow the “diffuse ISM approximation,” stating that all free electrons come from C II with an abundance of  $1.4 \times 10^{-4}$  (see Boersma et al. 2018, and references therein). Furthermore, we assume a standard power-law density profile for the globule,  $n_{\text{H}} \simeq n_0 \times (r/R)^{-1.3}$ , where  $r$  is the distance from the cloud center, and  $R = \sqrt{ab}$  is the effective radius of an elliptical cloud characterized by the major and minor semiaxes  $a$  and  $b$ ,

respectively. This, along with the values  $2a \simeq 0.9$  pc,  $2b \simeq 0.6$  pc, and the total mass of the cloud  $\simeq 160 M_{\odot}$  (Whittet 2007; corrected for the 435 pc distance), gives  $n_0 \sim 7 \times 10^3 \text{ cm}^{-3}$ , and hence  $n_e \sim 0.75 \text{ cm}^{-3}$ , around  $r \sim 0.45 \text{ pc} \gtrsim R$ .

Finally, for estimating the ionizing photon field for HD 130079, we take a stellar temperature of  $T_{\star} = 10,600$  K and a radius  $R_{\star} = 2.7 \times R_{\odot}$ , and assume a blackbody emission spectrum for the starlight

$$B_{\nu} \propto \frac{\nu^3}{\exp\left(\frac{h\nu}{kT}\right) - 1}, \quad (3)$$

such that the total luminosity of the star is  $L_{\star} = 4\pi R_{\star}^2 \sigma_{\text{SB}} T^4$ . This gives a far-UV (FUV) luminosity of

$$L_{\text{FUV}} = f_{\text{FUV}} \times L_{\star} \simeq 3 \times 10^{34} \text{ erg s}^{-1}, \quad (4)$$

where the bolometric correction factor is

$$f_{\text{FUV}} \equiv \frac{\int_{\nu_1}^{\nu_2} d\nu B_{\nu}}{\int_0^{\infty} d\nu B_{\nu}} \simeq 0.1 \quad (5)$$

with  $h\nu_1 = 6 \text{ eV}$  and  $h\nu_2 = 13.6 \text{ eV}$ . Consequently, at a given distance from the star  $d$ , where the FUV flux of the star is  $F_{\text{FUV}} = L_{\text{FUV}}/4\pi d^2$ , the ionizing photon field in Habing units

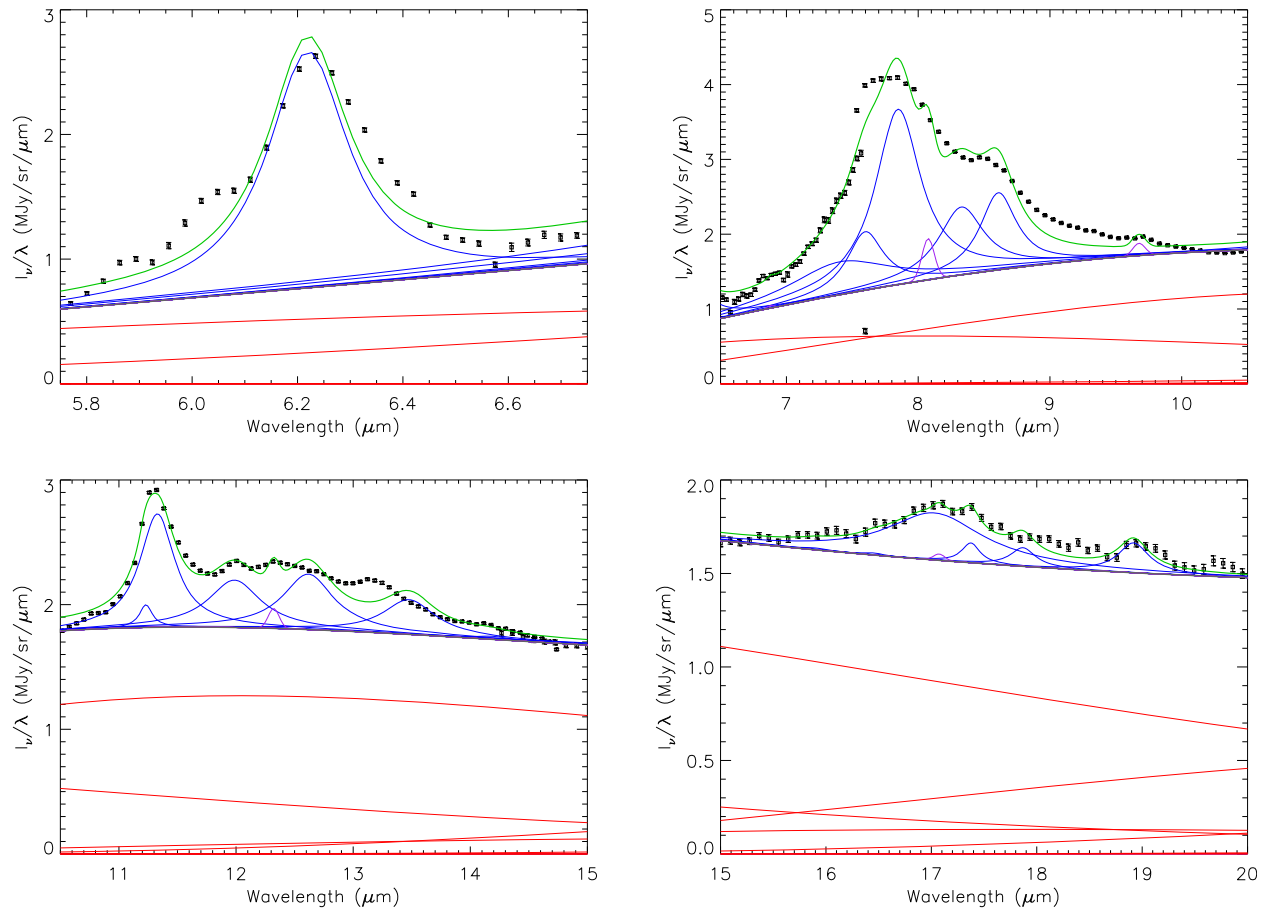


**Figure 9.** Zoomed-in view of spectral fit for the region located at a 0.03 pc projected distance from HD 130079 (see the upper panel in Figure 3, and also Figure 8). Lines and points are as defined in Figure 3, with the green solid line representing the fully fitted model.

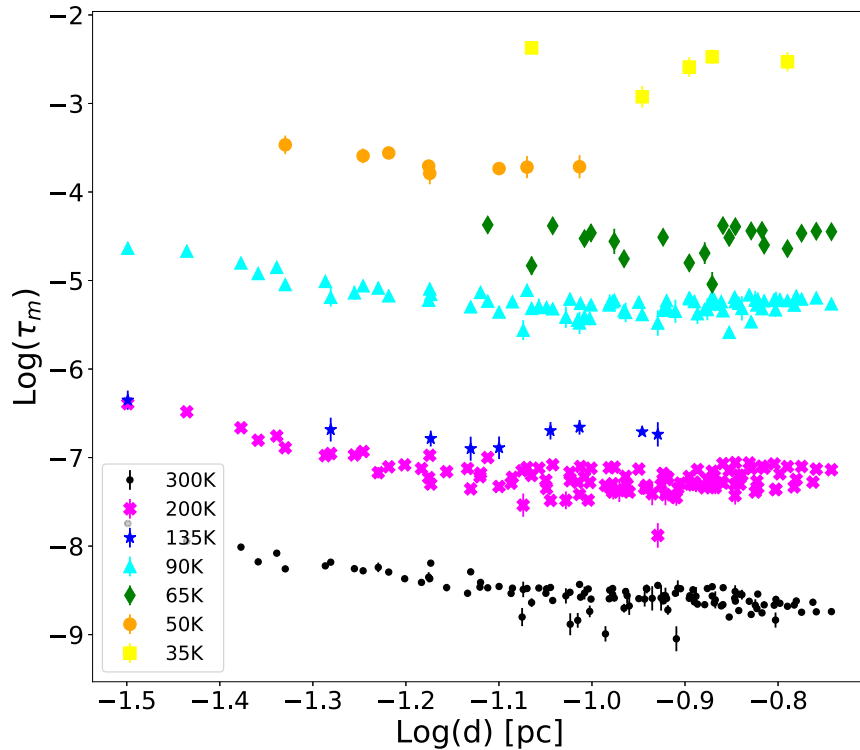


**Figure 10.** The relative strength of the dust continuum components with fixed model temperatures of 300, 200, 135, 90, 65, 50, 40, and 35 K, with increasing (projected) distance from the star HD 130079.



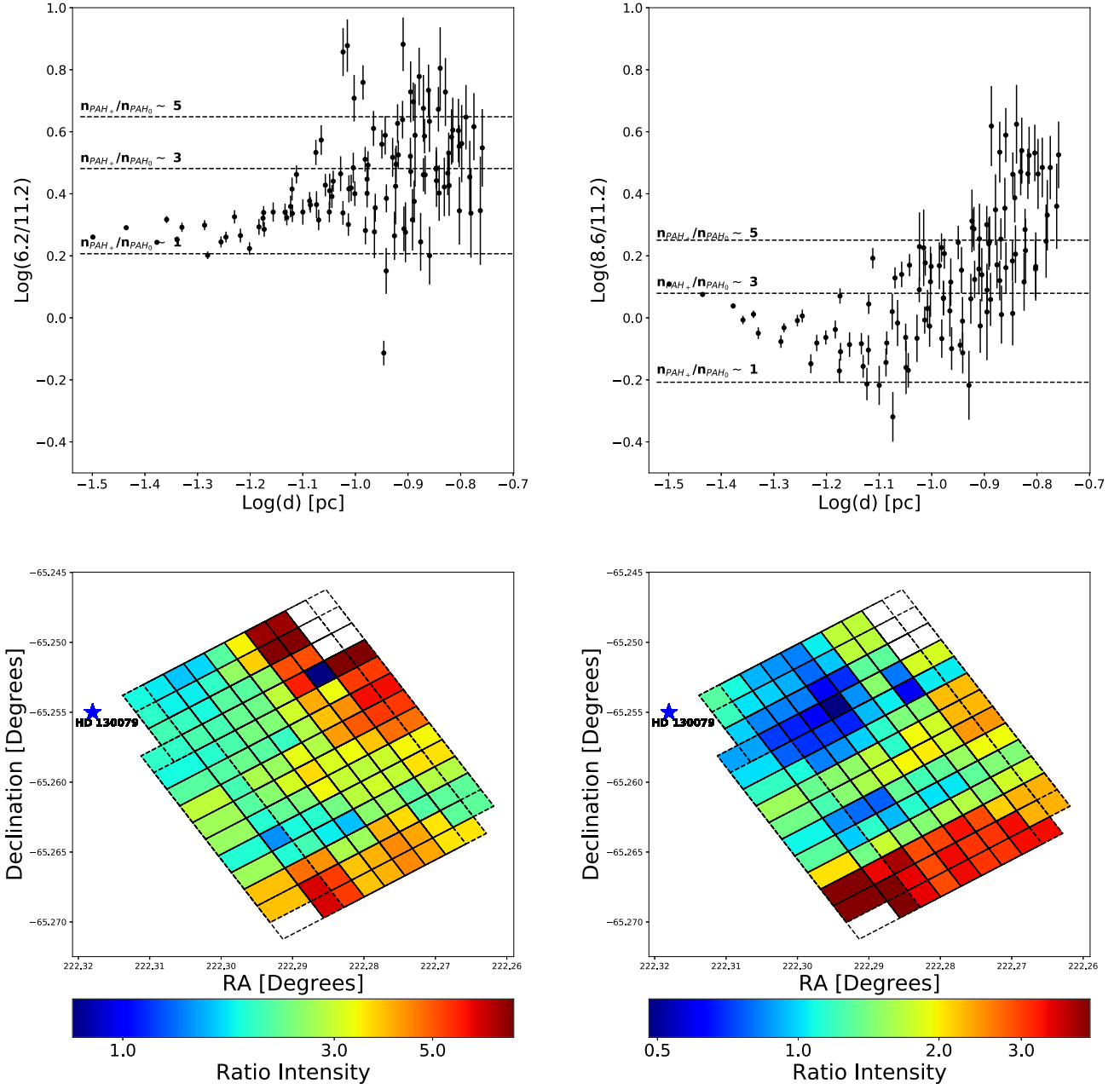


**Figure 11.** (Top panels) Diagrams showing the 6.2/11.2 intensity ratio (left) and 8.6/11.2 intensity ratio (right), based on the integrated profiles, vs. the projected distance from HD 130079. Horizontal lines correspond to the intensity ratios expected for given values of the ionization parameter  $n_{\text{PAH}^+}/n_{\text{PAH}_0}$ , based on the best-fit correlations by Boersma et al. (2018), namely  $I_{6.2\mu\text{m}}/I_{11.2\mu\text{m}} = 0.90 + 0.71 \times (n_{\text{PAH}^+}/n_{\text{PAH}_0})$ , and  $I_{8.6\mu\text{m}}/I_{11.2\mu\text{m}} = 0.33 + 0.29 \times (n_{\text{PAH}^+}/n_{\text{PAH}_0})$ . (Bottom panels) R.A./decl. maps displaying the 6.2/11.2 intensity ratio (left) and 8.6/11.2 intensity ratio (right).

reads as

$$G_0 = \frac{F_{\text{FUV}}}{1.6 \times 10^{-3} \text{ erg cm}^{-2} \text{ s}^{-1}} \sim 174 \quad (6)$$

for  $d = 0.03$  pc, which is the distance to the nearest sampled region to the star in DC 314.8–5.1. We note that  $G_0$  drops to  $\sim 4$  at the most distant region analyzed, at a distance of  $d \simeq 0.18$  pc (with no extinction correction taken into account).

All the above estimates therefore imply  $n_{\text{PAH}^+}/n_{\text{PAH}_0} \sim 0.5$  around the region nearest to HD 130079 in DC 314.8–5.1 ( $d = 0.03$  pc) for the general, illustrative value of  $N_{\text{C}} \sim 100$ , and progressively smaller levels away from the photoionizing star HD 130079. The resulting “outskirts-level” value is, in

fact, not far off from the PAH cation-to-neutral ratio,  $\gtrsim 1$ , implied for the region by the observed 6.2/11.2 PAH intensity ratio and the 8.6/11.2 line ratio, both considered by Boersma et al. (2018) to be good proxies for the ionized fraction parameter (see also Zang et al. 2019). However, the discrepancy between these values increases toward the globule’s central regions (up to  $d = 0.18$  pc), for which Equation (2) implies, formally,  $n_{\text{PAH}^+}/n_{\text{PAH}_0} < 0.01$ , while the observed PAH intensity requires this ratio to be of the order of a few.

To illustrate the abovementioned inconsistency, in Figure 11 we plot the 6.2/11.2 and 8.6/11.2 ratios (left and right columns, respectively) as functions of distance from the star; in the top panels, we superimpose for illustration the lines

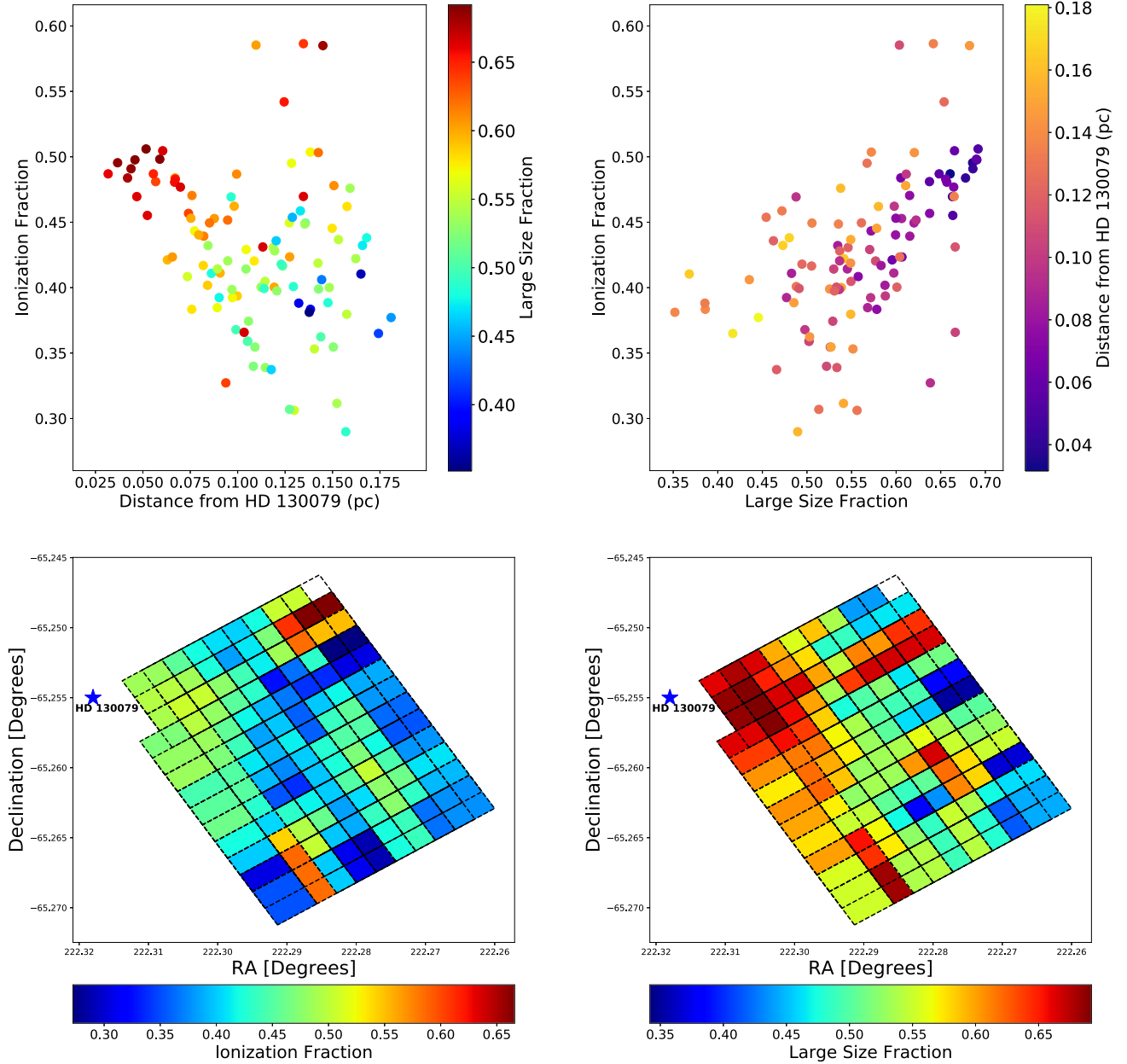


**Figure 12.** (Top left panel) The pyphadb values for the ionization fraction vs. distance with color coding according to the large-size fraction, where large molecules are defined to have  $N_C > 40$ . (Top right panel) The pyphadb values for the ionization fraction vs. large-size fraction with color coding according to the distance from HD 130079. The data points included are those from regions with  $S/N \geq 5$ . (Bottom) R.A./decl. maps displaying the intensity of (left) the ionization fraction and (right) the large-size fraction for the sampled regions.

corresponding to the intensity ratios expected for given values of the ionization parameter  $n_{\text{PAH}^+}/n_{\text{PAH}0}$ , based on the best-fit correlations by Boersma et al. (2018), namely  $I_{6.2\mu\text{m}}/I_{11.2\mu\text{m}} = 0.90 + 0.71 \times (n_{\text{PAH}^+}/n_{\text{PAH}0})$ , and  $I_{8.6\mu\text{m}}/I_{11.2\mu\text{m}} = 0.33 + 0.29 \times (n_{\text{PAH}^+}/n_{\text{PAH}0})$ .

As shown in Figure 11, both the 6.2/11.2 and 8.6/11.2 ratios remain relatively high throughout the globule, revealing similar trends, with the values increasing somewhat toward the central regions of the cloud (albeit with significant spread of data points). With the Boersma et al. scaling relation, this would imply an overall high ionization  $n_{\text{PAH}^+}/n_{\text{PAH}0} > 1$  within the entire reflection nebula.

The breakdown enabled by the pyphadb fitting offers a direct view of the ionization fraction within DC 314.8–5.1. As shown in Figure 12, the ionized fraction returned by the fitting

procedure,  $n_{\text{PAH}^+}/(n_{\text{PAH}^+} + n_{\text{PAH}0})$ , is  $\simeq 0.5$  within the regions of the cloud closest to the ionizing star, and decreases somewhat down to 0.3–0.4 at further distances, again with an increasing spread. These values therefore correspond to a ratio  $n_{\text{PAH}^+}/n_{\text{PAH}0} \simeq 1$  at the outskirts of the cloud, closer to the star, and down to  $\sim 0.5$ –0.7 at the furthest distances from the star probed in our analysis. Based on this, we therefore conclude that we do see an overall decrease in the ionization fraction with distance, which is however much more modest than expected based solely on the decrease in the ionizing continuum from the star, hinting at the potential role of alternative ionization factors at play, such as ionization due to cosmic rays.

Interestingly, the pyphadb fitting also provides insight into the large-size fraction of the PAH molecules, where large

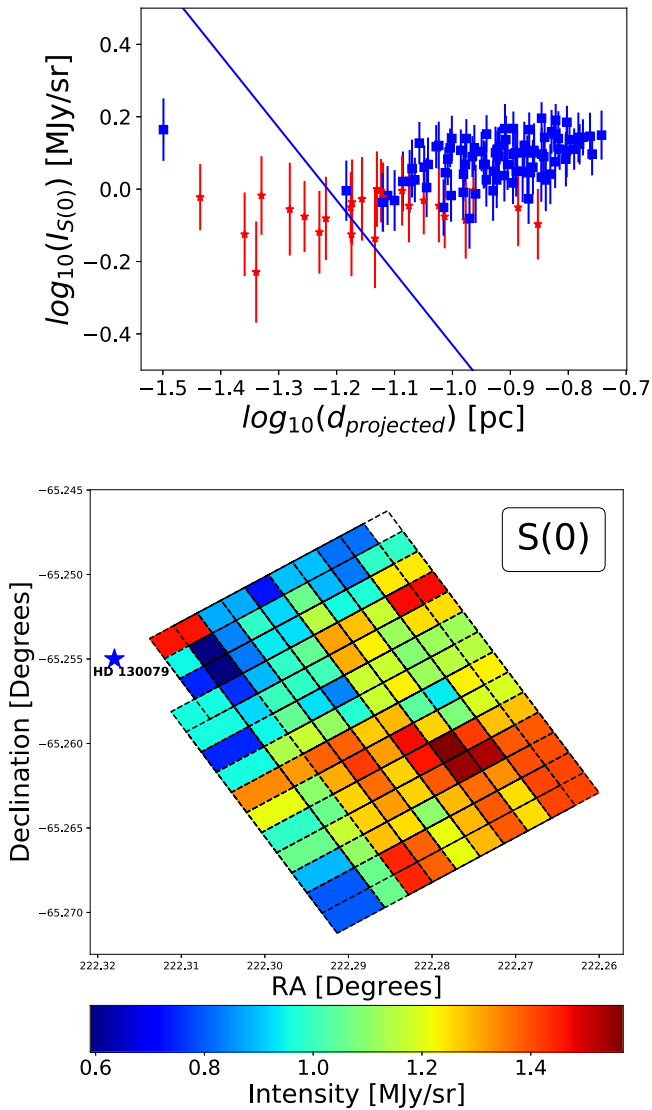


**Figure 13.** (Top) Logarithmic intensity of the  $\text{H}_2$  S(0) line located at  $28.1\text{--}28.2\ \mu\text{m}$  plotted with distance from the field star HD 130079. The blue line represents the inverse square scaling (with arbitrary normalization), to guide the eye. S/N is marked by color and symbol with red stars marking the lowest data points,  $3 < \text{S/N} < 5$ , and blue squares marking all data points with  $\text{S/N} > 5$ . (Bottom) R.A./decl. maps displaying the intensity of the fitted  $\text{H}_2$  S(0) line in each of the sampled regions with  $\text{S/N} > 3$ .

molecules are defined as those with  $N_C > 40$ . The corresponding results are again shown in Figure 12, revealing that the PAH emission of the highly ionized regions at the cloud’s boundaries is dominated by large molecules (large-size fraction  $> 0.6$ ), which become less prevalent for the regions closer to the center of the cloud (large-size fraction  $< 0.6$ ).

We furthermore perform a basic correlation study between the two parameters, the ionization and large-size fractions, over all of the sampled regions with  $\text{S/N} \geq 5$ , shown in the top right panel in Figure 12. We utilize both Pearson’s product moment correlation and Kendall’s rank correlation. We find a statistically significant correlation with both methods, showing a statistic of 0.56 and 0.45 and a  $p$ -value of  $1.2 \times 10^{-10}$  and  $3.6 \times 10^{-12}$  for Pearson’s and Kendall’s, respectively.

## 6.2. Molecular Hydrogen Detection

As shown in Figure 13, the  $\text{H}_2$  S(0) line is detected in our system at high significance ( $\text{S/N} > 5$ ) only at larger distances from the star. On the other hand, its intensity remains fairly constant throughout those outer regions probed in our analysis.

Excitation for  $\text{H}_2$  can occur through several processes, including inelastic collisions with gaseous species, radiative pumping from FUV radiation, and the formation process; the dominant source of the pure rotational line S(0) is collisional excitation, and as such the S(0) line intensity should be sensitive to the gas temperature at the PDR front (e.g., Le Boulart 1999; Neufeld & Yuan 2008; Habart et al. 2011).  $\text{H}_2$  excitation may however also result from interactions with secondary electrons generated by cosmic rays penetrating and ionizing the cloud (Wakelam et al. 2017).

## 7. Conclusions and Final Remarks

In this paper, we have discussed the MIR spectroscopic properties, provided by the IRS instrument on the Spitzer Space Telescope, of the quiescent dark cloud DC 314.8–5.1. This study has focused on the lower-resolution MIR spectra in the range of  $5\text{--}35\ \mu\text{m}$ . The spectra were extracted from 117 overlapping spatial regions over  $\simeq 0.18$  pc spanning the reflection nebula induced by the field star HD 130079. Spectral fitting revealed a plethora of PAH features, the inspection of which led to the following conclusions:

1. The intensities of PAH features generally decrease over distance from the ionizing star toward the cloud center, with some however showing a saturation (plateau) in the intensity profiles at larger distances.
2. The relative intensities of both the  $6.2$  and  $8.6$  features with respect to the  $11.2\ \mu\text{m}$  feature remain high throughout the globule, suggesting a relatively high cation-to-neutral PAH ratio  $\gtrsim 1$ . This value is consistent with the expected ionization level in the vicinity of the illuminating star, where the estimated ionization parameter  $\chi \sim 10^4$ ; however, for the cloud’s more central regions, where  $\chi$  drops to  $\sim 100$ , a discrepancy emerges between the expected value and the one implied by the observed PAH intensity ratio.
3. The performed pypahdb fitting confirms a high ionized fraction within the cloud, ranging from  $\simeq 0.5$  within the regions in the closest vicinity of the ionizing star, down to  $\sim 0.3\text{--}0.4$  at larger distances. Moreover, the PAH emission of the highly ionized regions at the cloud’s boundaries appears to be dominated by large molecules, which become less prevalent for the regions closer to the center of the cloud.
4. The investigation of the  $7.7\ \mu\text{m}$  profile in the reflection nebula of DC 314.8–5.1 shows that, in addition to the chemically processed PAH population of the cloud, we also see a fraction of PAHs UV-processed by the neighboring star, HD 130079.
5. We detect the  $\text{H}_2$  S(0) line at  $28.1\text{--}28.2\ \mu\text{m}$  with a higher significance at further distances from the star.

All in all, our results hint at divergent physical conditions within the quiescent cloud DC 314.8–5.1 as compared to molecular clouds with ongoing star formation, and this may suggest a role played by cosmic rays in the ionization of the system.






This work was supported by the Fulbright Program and was done in collaboration with the Astronomical Observatory of the Jagiellonian University. E.K. and Ł.S. were supported by Polish NSC grant 2016/22/E/ST9/00061. W.R.M.R. acknowledges financial support from the Leiden Observatory. A.K. acknowledges support from a First TEAM grant of the Foundation for Polish Science No. POIR.04.04.00-00-5D21/18-00. This article has been supported by the Polish National Agency for Academic Exchange under grant No. PPI/APM/2018/1/00036/U/001.

The authors thank A. Wójtowicz and D.C.B. Whittet for their discussion and comments. The authors also thank the anonymous referee for the critical remarks and constructive suggestions, which helped to improve the quality of the paper.

This work is based on observations made with the Spitzer Space Telescope, obtained from the NASA/IPAC Infrared Science Archive, both of which are operated by the Jet Propulsion Laboratory, California Institute of Technology, under a contract with the National Aeronautics and Space Administration.

This work has made use of data from the European Space Agency mission Gaia (<https://www.cosmos.esa.int/gaia>), processed by the Gaia Data Processing and Analysis Consortium (DPAC; <https://www.cosmos.esa.int/web/gaia/dpac/consortium>). Funding for the DPAC has been provided by national institutions, in particular the institutions participating in the Gaia Multilateral Agreement. We are grateful to Timo Prusti for advice on Gaia data.

### ORCID iDs

E. Kosmaczewski  <https://orcid.org/0000-0001-7150-4706>  
 Ł. Stawarz  <https://orcid.org/0000-0001-8294-9479>  
 W. R. M. Rocha  <https://orcid.org/0000-0001-6144-4113>  
 S. S. Shenoy  <https://orcid.org/0000-0003-0281-7383>  
 A. Karska  <https://orcid.org/0000-0001-8913-925X>

### References

Allamandola, L. J., Tielens, A. G. G. M., & Barker, J. R. 1989, *ApJS*, 71, 733  
 Bakes, E. L. O., & Tielens, A. G. G. M. 1998, *ApJ*, 499, 258  
 Bauschlicher, C. W., Ricca, A., Boersma, C., & Allamandola, L. J. 2018, *ApJS*, 234, 32  
 Bergin, E. A., & Tafalla, M. 2007, *ARA&A*, 45, 339  
 Berné, O., Joblin, C., Deville, Y., et al. 2007, *A&A*, 469, 575  
 Boersma, C., Bregman, J., & Allamandola, L. J. 2018, *ApJ*, 858, 67  
 Boersma, C., Bauschlicher, C. W., Ricca, J., et al. 2014, *ApJS*, 211, 8

Boogert, A. C. A., Chiar, J. E., Knez, C., et al. 2013, *ApJ*, 777, 73  
 Bregman, J. D., Allamandola, L. J., Tielens, A. G. G. M., Geballe, T. R., & Witteborn, F. C. 1989, *ApJ*, 344, 791  
 Bregman, J., & Temi, P. 2005, *ApJ*, 621, 831  
 Caselli, P., Keto, E., Bergin, E. A., et al. 2012, *ApJL*, 759, L37  
 Cernicharo, J., Bachiller, R., & Duvert, G. 1985, *A&A*, 149, 273  
 Chiar, J. E., Pendleton, Y. J., Allamandola, L. J., et al. 2011, *ApJ*, 731, 9  
 Dalgarno, A. 2006, *PNAS*, 103, 12269  
 Draine, B. T., & Li, A. 2001, *ApJ*, 551, 807  
 Gaia Collaboration, Brown, A. G. A., Vallenari, A., et al. 2021, *A&A*, 649, A1  
 Habart, E., Abergel, A., Boulanger, F., et al. 2011, *A&A*, 527, A122  
 Hartley, M., Manchester, R. N., Smith, R. M., Tritton, S. B., & Goss, W. M. 1986, *A&AS*, 63, 27  
 Herbst, E., & van Dishoeck, E. F. 2009, *ARA&A*, 47, 427  
 Hetem, J. C. G., Sanzovo, G. C., & Lépine, J. R. D. 1988, *A&AS*, 76, 347  
 Houck, J. R., Roellig, T. L., Van Cleve, J., et al. 2004, *Proc. SPIE*, 5487, 62  
 Indriolo, N., & McCall, B. J. 2013, *ChSRv*, 42, 7763  
 Indriolo, N., Neufeld, D. A., Gerin, M., et al. 2015, *ApJ*, 800, 40  
 Joblin, C., & Tielens, A. G. G. M. 2011, *EAS Publications Series*, 46, III  
 Kirk, J. M., Ward-Thompson, D., & André, P. 2007, *MNRAS*, 375, 843  
 Le Bourlot, J., Pineau des Forêts, G., & Flower, D. R. 1999, *MNRAS*, 305, 802  
 Li, A. 2020, *NatAs*, 4, 339  
 Maragkoudakis, A., Peeters, E., & Ricca, A. 2020, *MNRAS*, 494, 642  
 Micelotta, E. R., Jones, A. P., & Tielens, A. G. G. M. 2011, *A&A*, 526, A52  
 Neufeld, D. A., & Yuan, Y. 2008, *ApJ*, 678, 974  
 Padovani, M., Galli, D., & Glassgold, A. E. 2009, *A&A*, 501, 619  
 Peeters, E., Bauschlicher, C. W. J., Allamandola, L. J., et al. 2017, *ApJ*, 836, 198  
 Peeters, E., Hony, S., Van Kerckhoven, C., et al. 2002, *A&A*, 390, 1089  
 Pineda, J. L., & Bensch, F. 2007, *A&A*, 470, 615  
 Prasad, S. S., & Tarafdar, S. P. 1983, *ApJ*, 267, 603  
 Robitaille, T. 2019, APLpy v2.0: The Astronomical Plotting Library in Python, Zenodo, doi:10.5281/zenodo.2567476  
 Robitaille, T., & Bressert, E. 2012, APLpy: Astronomical Plotting Library in Python, Astrophysics Source Code Library, ascl:1208.017  
 Rosenberg, M. J. F., Berné, O., Boersma, C., Allamandola, L. J., & Tielens, A. G. G. M. 2011, *A&A*, 532, A128  
 Shannon, M. J., & Boersma 2018, Proc. of the 17th Python in Science Conf. (Austin, TX: SciPy), 99  
 Siebenmorgen, R., & Krügel, E. 2010, *A&A*, 511, A6  
 Skrutskie, M. F., Cutri, R. M., Stiening, R., et al. 2006, *AJ*, 131, 1163  
 Smith, J. D. T., Draine, B. T., Dale, D. A., et al. 2007a, *ApJ*, 656, 770  
 Smith, J. D. T., Armus, L., Dale, D. A., et al. 2007b, *PASP*, 119, 1133  
 Tielens, A. G. G. M. 2008, *ARA&A*, 46, 289  
 Verstraete, L. 2011, *EAS Publications Series*, 46, 415  
 Visser, R., Geers, V. C., Dullemond, C. P., et al. 2007, *A&A*, 466, 229  
 Wakelam, V., Bron, E., Cazaux, S., et al. 2017, *MolAs*, 9, 1  
 Ward-Thompson, D. 2002, *Sci*, 295, 76  
 Werner, M. W., Roellig, T. L., Low, F. J., et al. 2004, *ApJS*, 154, 1  
 Whittet, D. C. B. 2007, *AJ*, 133, 622  
 Whittet, D. C. B., Gerakines, P. A., Hough, J. H., & Shenoy, S. S. 2001, *ApJ*, 547, 872  
 Whittet, D. C. B., Poteet, C. A., Chiar, J. E., et al. 2013, *ApJ*, 774, 102  
 Zang, R. X., Peeters, E., & Boersma, C. 2019, *ApJ*, 887, 46